Two-Phase CFD and PIV EFD for Plunging Breaking Waves, Including Alternative CFD Approaches and Extensions for Air/Water Ship Flow

F. Stern[1], J. Huang[1], P. Carrica[1], J. Yang[1], S. Ghosh[1], S. Van[2]
([1]University of Iowa, Iowa City, IA 52242, USA; [2]Maritime and Ocean Engineering Research Institute, Korea)

ABSTRACT

This paper represents a first step towards the development of two-phase CFD methods for small and large scale ship hydrodynamic applications. Two-phase level set approaches are being implemented in CFDShip-Iowa to extend the modeling capabilities of the current version 4 along with complementary experiments for validation. The experiments are conducted in an open channel flume using bottom mounted bumps to generate plunging breaking waves. Experimental work includes determining the optimum flow conditions for generating periodic and impulsive plunging breaking waves, theoretical analysis for free surface instabilities that are observed at low speeds prior to the breaking process, and experimental measurements for validation of the theory. Two two-phase level set methods, the Heaviside function method (HFM) and the ghost fluid method (GFM) are extended to curvilinear body-fitted grids to simulate air/water free surface turbulent flows and the methods are applied to plunging wave breaking, sub-critical free surface flows generated by a submerged bump, and free surface turbulent flow both in air and water around a ship model DTMB 5512. The results show good agreement with experimental data. Another method using two-phase level set embedded boundary Cartesian grid, has also been implemented and results are presented for some preliminary computations. The simulation of impulsive plunging breaking waves is in very good qualitative agreement with the experimental data. A computation of non-breaking waves generated by a submerged hydrofoil has also been carried out and the results compared very well with the experimental data.

INTRODUCTION

Two-phase CFD methods are needed for both small and large scale ship hydrodynamics applications. Detailed resolution of both air and water phases is important for prediction at the smaller scales of steady and unsteady breaking waves (including splashing, free surface turbulence, and bubble entrainment) and wind-wave interactions. At the larger scales, the effects of superstructure forces and air wakes and their interactions with wave and water flow as well as air pressurization in compartments are also of importance. Current surface tracking and single phase level set approaches are not able to handle such problems, which require simultaneous solutions of air and water flows. Two phase level set approaches in principle can. However, relatively little attention has been given to the detailed air/water flow, except for investigations of two-dimensional unsteady wave breaking or three-dimensional super structure air wakes without consideration to the free surface and waves. Additionally, detailed experiments for physics, model development, and CFD validation for unsteady breaking waves and air/water ship flows are lacking.

This paper represents a first step towards the development of two-phase CFD methods for such problems and complementary PIV EFD with specific focus on the investigation of plunging breaking waves, alternative CFD approaches, and extensions for air/water ship flow. Plunging breaking wave experiments are conducted in an open channel flume over curved bumps for both periodic and impulsive breakers, including in the former case the identification of three-dimensional span wise instabilities and their theoretical prediction derived using centrifugal instability analysis and validation using present EFD data. Two two-phase level set methods are implemented in CFDShip-Iowa version 5.0 [i.e., curvilinear solvers and classic heaviside function method (HFM) and ghost fluid method (GFM)] and tested for submerged bumps using both available EFD data for non-breaking waves and using the present EFD data for impulsive plunging breaking waves and for air/water ship flow using previous IIHR EFD data for 5512. Two-phase HFM is implemented in a Cartesian solver, immersed boundary CFD code and tested for submerged bump using the present EFD data for impulsive plunging breaking waves and for submerged

hydrofoils using available EFD data. Coupling of Cartesian solver for outer flow and curvilinear solver for inner flow near solid boundaries is the envisioned approach for CFDShip-Iowa version 6.0. In the following, appropriate background discussions with references are provided for each investigation followed by descriptions of EFD or CFD methods and results. Lastly, concluding remarks are made, including discussion of pros and cons of alternative CFD approaches and future work for both CFD and EFD.

PLUNGING BREAKER EXPERIMENTS

Background

Water waves have always been an interesting topic of research for many scientists for centuries. One of the most important and complex features of water waves is the wave breaking process itself that can occur in both deep water and shallow water regions of the oceans and can affect ships, trawlers, coastal structures etc. Ship bow wave breaking is the major concern of this research. Although there is a dearth of available experimental data for bow wave breaking, the structure of the wave has received considerable attention over the years as summarized in a comprehensive review by Miyata & Inui (1984). They had demonstrated that the near surface flow becomes turbulent downstream of the wave crest. Due to limitations in their technique they were unable to measure velocity and turbulent fields in the immediate vicinity of the wall and free surface. Dong et. al. (1997) had performed PIV measurements on a ship model and found that a shear layer is formed at the toe of the breaking wave that extends into the fluid. Pogozelski et. al. (1997) obtained PIV measurements of the flow around a towed blunt body and had observed weak breaking at the bow wave but still saw generation of negative vorticity close to the forward face unlike a two dimensional breaking wave in which an extended shear layer is formed as reported by Lin & Rockwell (1995).

Even though several researchers have made laboratory as well as field measurements to understand the process of wave breaking and its effects, it is still a very complex phenomenon, the physics of which needs to be fully understood, especially to improve the design of ships and offshore structures that are exposed to extreme conditions. Of all kinds of breaking, plunging is the most dramatic wave breaking phenomenon and the first part of this manuscript focuses on understanding the evolution, instabilities that lead to wave breaking and finally the breaking process of a plunging wave breaker through laboratory experiments.

Test plan & flow conditions

The present experiments are motivated to study breaking waves and obtain validation data for two

phase CFD results. The first step was to generate plunging breakers with typical characteristics of overturning of crest, splashing and air entrapment, devoid of any surface tension effects. Peregrine (1983) introduced the criteria that waves steeper than 10 cm are not affected by surface tension which inhibits both plunging and air entrapment. Experiments were conducted in two open channel flumes with curved bumps fixed to the flume bottom surface, that were used to generate plunging wave breaking. Two different bump geometries (semicircular and fourth order curvature profile) were used for different bump heights. The water depths and the flow speeds for each bump were varied to generate the best case of plunging breaking. The aim was to create plunging breakers larger than 10 cm wave height. The test plan is given in Table 1.

Table 1: Test conditions for breaking waves

Flume 1 – Semicircular bumps			
	h (cm)		
H = 10.80 cm	2.54	7.62	10.16
H = 16.18 cm	2.54	3.81	5.08
H = 20.30 cm	2.54	3.81	5.08
H = 27.94 cm	2.54	3.81	5.08
Flume 2 – Semicircular bumps			
	h (cm)		
H = 25.40 cm	2.54	3.81	5.08
H = 27.94 cm	2.54	3.81	5.08
H = 31.80 cm	2.54	3.81	5.08

Flume 2 – Bumps with fourth order curvature profile					
	h (cm)				
H = 9.14 cm	1.27	2.54	3.81	5.08	11.43
H = 11.43 cm	1.27	2.54	3.81	5.08	11.43
H = 13.97 cm	1.27	2.54	3.81	5.08	11.43
H = 27.94 cm	1.27	2.54	3.81	5.08	-

Note: H is the bumpheight; h is the depth of water above the bump. Flume 1 is 9m long, 0.6m wide and 0.55m deep and Flume 2 is 18m long, 0.9m wide and 0.55m deep

During the course of initial experiments, two different kinds of plunging breakers were identified. It was found that if the water depths above the bump (h) was kept below 6 cm and the upstream speed was in the range of 5-25cm/s, the wave breaking occurred repeatedly downstream of the bump and was highly three dimensional with significant span-wise variation. With higher values of h (h ~ 11cm) and increased upstream flow speed of 0.7m/s, two dimensional plunging breakers could be created. The former kind of wave breaking was dominated by the span-wise instability on the free surface. Both theoretical analysis and experimental measurements were performed to find a critical number that defines the onset of this instability. Flume 2 was chosen finally for both instability and wave breaking measurements, since it has larger aspect ratio which reduces the effect of side walls.

Instability analysis & validation

Three dimensional span-wise instabilities have been observed at the free surface for spilling and plunging breaking waves in both deep and shallow water. These instabilities (figure1) resemble longitudinal braids spanning across the width of the wave. Even though detailed studies of these instabilities have not been done yet, there have been anecdotal reports of its observations in laboratory experiments related to wave breaking also. Perlin et. al. (1996) had performed experimental studies on plunging breakers and had observed instabilities that resembled capillary waves in the transverse direction along the forward portion of the plunging jet, but they did not include any detailed study of the instabilities. Steinbach et. al. (2002) had studied the cross-stream crest profiles of spilling breakers and had observed ripples that were generated upstream of the crest that were presumably due to the rapid development of stream-wise vorticity.

The present experiments are motivated to study breaking waves and obtain validation data for two phase CFD results. In the process of determining the best conditions for wave breaking, span-wise instabilities are observed at the free surface that inspires the authors to make a separate detailed study of these instabilities. The span-wise instabilities are caused by stream-wise vortices downstream of the bump and seem to be fortuitously accentuated by the experimental setup making them very distinct and larger than capillary waves and can possibly be related to real life wave instabilities on beaches and around ships or other ocean structures. After thorough observations and experimental measurements with different bump sizes and different water depths, it is concluded that this instability at the free surface is caused due to the centrifugal force that is generated by the flow accelerating over the bump which causes stream-wise vorticity downstream of the bump.
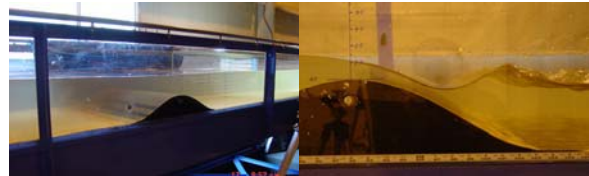

Figure 1. Front view of spanwise instability on a shallow-water breaking wave on the beach, arrows highlighting width of instability (Miami, USA, 12.31.2005).

However, previous studies of bluff body flows (Williamson, 1996) have shown that there can be other sources of stream-wise vorticity in bluff body wakes. The first kind is due to the three dimensional instability of Karman vortices, e.g. in circular cylinder flows and the second kind is due to the secondary vortices from the separating shear layer from the sides of the cylinder. The following section discusses the relative importance of these secondary stream-wise structures compared to the centrifugal instability for the bump flow using theoretical analysis and experimental data and establishes the fact that the free surface instability downstream of the bump is due to the centrifugal stream-wise vortices only and not due to any other vorticity source.

The purpose of the first part of this manuscript is to derive a non dimensional critical number that determines the onset of this free surface instability using theoretical analysis similar to Taylor-Couette flow for concentric rotating cylinders and validating theoretical results by experimental data.

Experimental setup and flow conditions. In the experimental setup (figure 2a) a curved bump profile, chosen according to Iafrati et. al.(2001), is fixed to the bottom of an open channel flume, 27m long, 0.91m wide and 0.43m high. The water depth above the bump (h) is varied as well as the flow speed to generate breaking waves downstream of the bump.

Figure2. Open channel flume with curved bump fixed to the bottom (left). Side view of the flow (right).
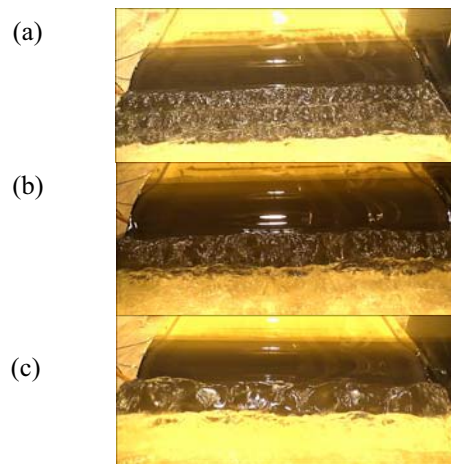
Figure 3. Top view of span-wise instability (a) h/H = 0.111 cm. (b) h/H = 0.222 cm. (c) h/H = 0.333 cm.

A concave region is formed immediately downstream of the bump before the first wave (figure 2b) that is generated due to the acceleration of the flow

over the bump. It is observed that for low water depths above the bump (h < 6cm) and low upstream speeds ($U_\infty \sim$ 1-17 cm/s) the free surface instabilities occur downstream of the bump. Figure 3 shows top view of the span-wise instability looking from downstream side of the flow for varying water depths above the bump.

Table 2 summarizes the different experimental flow parameters and conditions for 11.43cm bump. The span-wise wavelength of the instability, which is equal to the width of the longitudinal braids seen at the free surface, for different water depths are measured from video images of the free surface with reference scales. Since the minimum Weber number is 159 the effects of surface tension are negligible. The maximum Reynolds number is 12878 and so the whole experiment is carried out at sub-critical flow regime.

Table2. Flow conditions

Bump height (H) = 11.43 cm			
h/H	Re_∞	We	w_T/W
0.056	990	159	0.006
0.111	2034	1002	0.011
0.222	5425	1693	0.035
0.333	8633	5043	0.060
0.444	12878	7079	0.120

Note: W is the flume width. w_T is half of the span-wise wavelength of free surface instability. Re_∞ is the Reynolds number based on the upstream flow speed and bump height,. $We = \rho V_1^2 R_1/Y$, where, V_1 is the free surface velocity at the concave region, R_1 is the radius of curvature of the concave region and Y is the surface tension.

Figure 4 shows the schematic illustration of the flow over the bump. The flow separates from the bump surface forming a separation streamline (figure 4a) thus creating a separation bubble below it at a certain distance below the free surface. R_1 and R_2 are the radii of curvatures of the free surface and the separation line respectively. The distance between free surface and separation line is d. The angular velocity at the free surface in the concave region is defined as Ω_1, and Ω_2 is the angular velocity at the separation line. Cylindrical coordinate system is chosen to define the flow with r and θ as shown on the figure, and z being the transverse direction out of the plane of the figure. The free surface instability originates at the concave region from the trough before the first wave and is caused by stream-wise vortices that also start to develop from the same location underneath the free surface.

The theoretical analysis for the mean flow is based on three major assumptions that enable to simplify the overall problem formulation. Introduction of dye upstream of the bump clearly shows the separation streamline having similar shape as the free surface downstream of the separation point without any radial flow and at the free surface the flow is quite steady without any vertical oscillations. It follows that within a small region in the narrow gap just downstream of the separation point and upstream of the region where the instability first sets in, the flow can be assumed to be purely circumferential. Secondly, it is assumed that the flow is mainly two-dimensional just upstream of the instability and so the span-wise component of velocity is negligible. The third one assumes constant pressure along the separation line very close to the separation point due to the presence of separation bubble below the separation line. It is quite well known that the pressure within the separation bubble for cylinder flow is constant and has been verified by Kirkil & Constantinescu (2006) and hence assuming constant pressure along the separation line close to the bump is a valid assumption.

This kind of flow is found to be analogous to Taylor-Couette flow with concentric cylinders and the inner cylinder rotating at a higher angular velocity. For the present setup the free surface having higher angular velocity acts as the inner cylinder, the separation line acts as the outer cylinder with lower angular velocity and the gap width (d) is similar to the gap between concentric cylinders. Figure 4b shows the schematic of the cross sectional view at the first trough and shows the flow pattern with dominant large scale centrifugal stream-wise vorticity. Figure 4c shows the smaller scale secondary vortices at the crest of the primary wave generated from the separating shear layer. The ratio of centrifugal vortices to shear layer vortices shown in figure 4c is applicable for water depth h/H = 0.333. For other water depths the relative sizes of centrifugal and shear layer vortices vary.
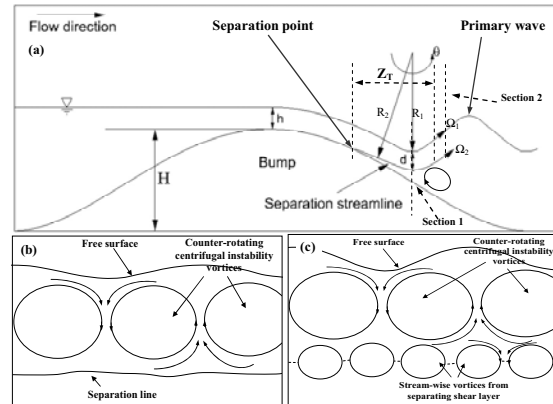

Figure 4. A schematic illustration of the flow. (a) Side view of the flow (b) Cross sectional view of the flow at the trough (section 1). (c) Cross sectional view of the flow at the first crest (section 2).

Review of stream-wise structures in the wake of circular cylinders. Williamson (1996) discussed that for flow behind a circular cylinder within a range of $1200 < Re_\infty < 200000$, there are two

different phenomena that can cause stream-wise vorticity in the wake.

The first kind of stream-wise vorticity is independent of the Reynolds number within that range and is generated from the braid regions of Karman vortices having a span-wise wavelength almost equal to the cylinder diameter. Mansy et. al. (1994) found out from their experiments that these stream-wise vortices develop at around a downstream distance of ten times the cylinder diameter. The present experiments are conducted at a range of $990 < Re_\infty < 12877$. However, in the present flow the span-wise wavelength of the free surface instability varies with water depth and does not scale with the bump height. Besides, the free surface instability originates from the trough just downstream of the bump which is approximately at a distance of half the bump height from the separation point. This implies that the free surface instability behind the bump is definitely not caused due to the three dimensional instability of Karman vortices.

The second source of stream-wise vorticity is the separating shear layer that originates from the sides of the cylinder. Williamson (1996) estimated the length scales of the shear layer stream-wise vortices given as follows:

$$\lambda_{SL} = 25 D_c / Re_\infty^{1/2} \qquad (1)$$

where, λ_{SL} is the span-wise wavelength of stream-wise vortices generated from the shear layer instability and D_c is the cylinder diameter. Sato (1956) suggested that for this shear layer instability to appear in the near wake, a significant amplification of the instability is reached only after a transition distance of,

$$Z_T \sim 75 D_c / Re_\infty^{1/2} \qquad (2)$$

For the present set of experiments the shear layer is generated from the separation streamline. Digital PIV measurements in the transverse plane have shown evidence of large scale stream-wise vortices in between the free surface and separation line right at the trough that are caused by centrifugal instability. The theoretical values of the sizes of the shear layer vortices based on the different critical Reynolds numbers are smaller than the stream-wise vortices measured at the trough, and their wavelengths do not match the free surface span-wise wavelength either, which indicates that these shear layer vortices are much smaller compared to the ones that cause the free surface instability. Table 3 summarizes the comparison of the centrifugal vortex sizes measured at the trough with secondary shear layer vortices that are measured from experiments and also estimated using equation (1). For $h/H = 0.056$, since the Reynolds number is less than 1200, equation (1) is not applicable. The theoretical analysis for shear layer vortices is only applicable for infinite water depth flows. For water depth $h/H = 0.111$, since the level is too shallow, equation (1) is probably not applicable either and so we see that the predicted theoretical value of shear layer vortices is larger than centrifugal vortices, even though experimental values are lower. For all other cases both the experimental and estimated theoretical values of shear layer vortices are smaller than the centrifugal vortices. It is interesting to note that the sizes of shear layer vortices measured from experimental data (w_{SLE}) compare well with the theoretical values (w_{SLT}) for higher water depths. This is reasonable since increasing water depth means reduced free surface effect. As mentioned before PIV measurements have shown evidence of stream-wise vorticity right at the trough which is upstream of the transition distance for most water depths. Subsequent PIV measurements downstream of the transition distance show evidence of the shear layer vortices near the separation line and well below the free surface. This implies that even though the shear layer stream-wise vortices are present below the free surface downstream of the trough, the free surface instability that originates at the trough is not caused by them. It is also interesting to note that theoretically shear layer stream-wise vorticity cannot be present for the lowest water depth with $Re_\infty = 990$, since at that Reynolds number shear layer vortices are not known to exist according to Williamson (1996), but the free surface instability is still clearly visible.

Table3. Comparison of vortex sizes for 11.43 cm bump.

h/H	Re_∞	Z_T/H	w_T/W	W_{SLE}/W	W_{SLT}/W
0.056	990	2.38	0.006	-	0.049
0.111	2034	1.66	0.011	0.001	0.034
0.222	5425	1.02	0.035	0.006	0.021
0.333	8633	0.81	0.060	0.009	0.015
0.444	12878	0.66	0.120	0.012	0.012

Note: w_{SLE} is width of secondary shear layer vortex obtained from experiments, and w_{SLT} is the theoretical value of shear layer vortex width calculated using equation (3.1).

Figure 5 shows the effect of upstream flow speed on the width of span-wise instability observed at the free surface maintaining the water depth above the bump constant, starting from critical condition. At the critical condition the vortices are just starting to develop and so the width of the span-wise instability is not clearly noticeable in figure 5a, however at higher speeds (figures 5b, 5c and 5d) it is quite evident that the instability is well developed and the vortex width is independent of the flow speed and remains constant till the point when the primary wave starts to break. Centrifugal theoretical analysis predicts that the vortex size depends on the gap width between free surface and separation line and is independent of the flow speed similar to Taylor-Couette flow. If the free surface

instability is caused by the shear layer vortices, then according to equation (1) increasing the flow speed would have reduced the vortex sizes which is not observed.
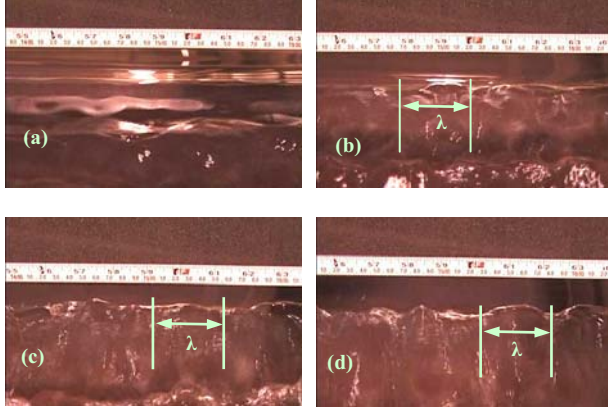
Figure 5. Variation of width of instability (11.43cm bump) at the free surface with increasing upstream flow velocity for h = 2.54cm (a) Critical condition (Re_∞ = 5425). (b) Re_∞ = 6408. (c) Re_∞ = 7368. (d) Re_∞ = 7871.

Considering all the above experimental observations and theoretical arguments, it is concluded that the free surface instability is caused only due to the centrifugal force effect, however the shear layer vortices are also present below the free surface for the cases where Re_∞ is higher than 1200, and develop only after the transition distance and their existence makes the flow even more interesting. The following section presents the theoretical analysis for the centrifugal instability observed at the free surface.

Theoretical analysis. Present study focuses on solving the mean flow and perturbation equations for flow behind the bump with suitable boundary conditions following similar method as Taylor instability analysis for viscous Couette flow investigated by Chandrasekhar (1961), and obtaining experimental data to validate theoretical analysis for centrifugal instability.

Mean flow equations. Continuity and Navier-Stokes equations in cylindrical polar coordinates, for viscous incompressible flow are used for theoretical analysis. The equations can be converted to dimensionless form using the following definitions,

$$u^* = u/U; r^* = r/R; p^* = p/\rho U^2; t^* = R/U; \quad (3)$$

where, U and R are characteristic velocity and length scales respectively. The non-dimensional Continuity equation is given as follows:

$$\frac{1}{r^*}\frac{\partial}{\partial r}\left(r^* u_r^*\right) + \frac{1}{r^*}\frac{\partial}{\partial\theta}\left(u_\theta^*\right) + \frac{\partial}{\partial z^*}\left(u_z^*\right) = 0; \quad (4)$$

(3.11)

The flow is mainly two-dimensional just upstream of the instability and so the z – component of velocity and gradient vanishes. Since the flow is assumed to be purely circumferential and so u_θ^* is only a function of r^*.

$$u_\theta^* = F(r^*) \text{ since, } \frac{1}{r^*}\frac{\partial}{\partial\theta}\left(u_\theta^*\right) = 0 \quad (5)$$

The non-dimensional r-momentum equation is given below..

$$\frac{\partial p^*}{\partial r^*} = \frac{u_\theta^{*2}}{r^*} + \frac{gR}{U^2}\cos\theta \quad (6)$$

Integrating equation (6) with respect to r^* we obtain,

$$p^* = \int\frac{u_\theta^{*2}}{r^*}dr^* + \frac{gR}{U^2}r^*\cos\theta + K_1; \quad (7)$$

K_1 is the constant of integration that is determined from pressure boundary conditions. At the free surface, $r^* = R_1^*$, Y is the surface tension and We is the Weber number.

$$p^* = \frac{P_a}{\rho U^2} - \frac{Y}{\rho U^2 R_1} = \frac{P_a}{\rho U^2} - \frac{1}{We}, \quad (8)$$

At the separation streamline, $r^* = R_2^*$, and

$$p^* = p_2/\rho U^2, \quad (9)$$

where, p_2 is the pressure at the separation line. Surface tension effects are negligible as discussed before so the Weber number term can be neglected. Since the pressure along the separation line is assumed constant, p_2 is independent of θ, close to the separation point. So the constant K_1, is independent of θ. Differentiating p^* with respect to θ we obtain,

$$\frac{\partial p^*}{\partial\theta} = -\frac{gR}{U^2}\sin\theta; \quad (10)$$

The non-dimensional form of θ – momentum equation is given by,

$$\frac{\partial u_\theta^*}{\partial t^*} = -\frac{1}{r^*}\frac{\partial p^*}{\partial \theta} - \frac{gR\sin\theta}{U^2} +$$
$$\frac{v}{UR}\left(\frac{\partial^2 u_\theta^*}{\partial r^{*2}} + \frac{1}{r^*}\frac{\partial u_\theta^*}{\partial r^*} - \frac{u_\theta^*}{r^{*2}}\right); \qquad (11)$$

Assuming steady state flow, and substituting equation (10) in (11) we obtain,

$$\frac{\partial^2 u_\theta^*}{\partial r^{*2}} + \frac{1}{r^*}\frac{\partial u_\theta^*}{\partial r^*} - \frac{u_\theta^*}{r^{*2}} = 0; \qquad (12)$$

The solution to equation (12) gives

$u_\theta^* = A^* r^* + B^*/r^*$; where A^* and B^* are constants that need to be determined. Reverting back to dimensional form we can express the velocity profile as given below,

$$u_\theta = Ar + B/r; \ \Omega = A + B/r^2; \qquad (13)$$

where, the constants A and B are determined from the following boundary conditions:
$du_\theta/dr = 0$, at $r = R_1$ due to zero shear stress at the free surface, and, $u_\theta/r = \Omega_2$, at $r = R_2$. This gives,

$$A = \Omega_2/(1+\eta^2), B = R_1^2 \Omega_2/(1+\eta^2), \qquad (14)$$
where, $\eta = R_1/R_2$

If the angular velocity at the free surface is defined as Ω_1, then we get another relation given by

$$\Omega_1 = A + B/R_1^2 \qquad (15)$$

Substituting the values of A and B from equation (14) in (13) we can obtain a unique relation between the angular velocities at the free surface and separation line in terms of η as given below,

$$\Omega_2/\Omega_1 = \mu = (1+\eta^2)/2 \qquad (16)$$

Perturbation equations. Chandrasekhar (1961) had presented experimental results for both narrow (gap width is less than 5% of the mean of radii) and wide gap Taylor-Couette flow. In the present setup for all experimental cases, the gap width ($d = R_2-R_1$) is

less than 5% of the mean radii and so narrow gap assumption is used for solving the perturbation equations.

Reid (1960) has shown that we can assume linear profile for angular velocity for narrow gap case for inviscid Couette flow. Figure 6 shows the angular velocity profiles for the present problem for both narrow and wide gap cases. It can be clearly seen from figure 6a, that using linear angular velocity profile within the gap for viscous flow over the bump is a justified assumption.
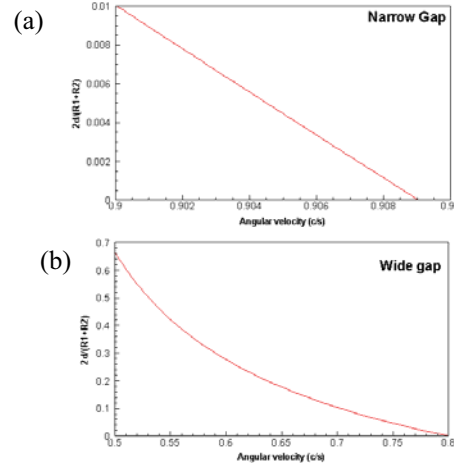
Figure 6. Angular velocity profiles between free surface and separation line (a) Narrow gap profile. (b) Wide gap profile

Assuming that the perturbations are also circumferential and independent of θ, and following the exact same method as described in Chandrasekhar (1961), the expression for critical Taylor number is given as follows:

$$T = \frac{8A\Omega_2 d^4}{v^2}\frac{\eta}{2\eta-1} = \frac{8\Omega_2^2 d^4 \eta}{(1+\eta^2)(2\eta-1)v^2} \qquad (17)$$

where, T is the critical Taylor number.
The boundary conditions for the perturbation equations are given below:
1. $Du = Dv = Dw = 0$ at the free surface due to zero shear stress, where, u, v and w are the perturbations in the r, θ, z directions respectively and $D = d/dr$.
2. $u = Du = 0$ at the separation line, since the flow is assumed to be fully circumferential within the gap.
3. v is non zero at the free surface and also on the separation line.
The perturbation equations have been solved in the same way as described in Chandrasekhar (1961) and hence the detailed steps of solution have not been presented here. The final expression for Taylor number

as a function of non-dimensional wavelength of instability is given as,

$$T = -\frac{4\psi}{a\left[\begin{matrix} 4a^2\psi^3\{A_1\sinh a + B_1(1+\cosh a)\}+(2+\alpha)+ \\ 2a\psi^3\left[\begin{matrix}\{A_2\sinh a + B_2\cosh a\}+ \\ \psi(\pi^2-a^2)\{A_2(1+\cosh a)+B_2\sinh a\}\end{matrix}\right]\end{matrix}\right]}$$

(18)

where, T is the Taylor number, $\alpha = (1-1/\eta)/2$, λ is the span-wise wavelength of instability, $a = 2\pi d/\lambda$, $d =$ gap width and $\psi = 1/\pi^2 + a^2$;

Experimental results. After comparing the flow qualities with different bump sizes and geometries, a bump with fourth order curvature profile and height of 11.43cm is chosen for instability studies. Instability experiments are conducted by varying the initial water depth (h) above the bump as well as the upstream flow speeds. The experimental setup is shown in figure 7.

The water depth above the bump is increased from a minimum value of 0.635 cm to a maximum of 5.08 cm and measurements are obtained for each depth. The flow velocity is set at a value where the instability first appears downstream of the bump to set the critical condition. For comparing theoretical critical Taylor number with experimental data, the gap width (d), the width of the vortex (w_T), the radius of curvature of the free surface (R_1) at the concave region and the angular velocity (Ω_2) at the separation line are measured for each water depth at the critical condition. For each water depth, three overall sets of measurements are obtained. Results presented here are the mean of three sets.

Wave gauge is used to measure the free surface elevation profiles at the concave region for calculating the radius of curvature at the free surface (R_1). A single servo mechanism wave probe (30cm needle with 1200mm/s response time) is mounted on a 1D traverse which is free to move in the stream-wise direction. Surface flow system is used to measure the stream-wise velocity components that are obtained at the same concave region on the free surface only for the lowest water depth. Since the gap width is very small in this case, it is difficult to measure the velocity at the separation line directly. The free surface velocity, V_1 is used to estimate the velocity at the separation line using equation (15), instead of direct measurement. Digital PIV is used to obtain cross-plane velocity vectors and vorticity. The setup is shown in figure 7b.

Still photographs (figure 8a) of free surface instability are obtained with reference scales to estimate the width ($w_T = \lambda/2$) of the centrifugal instability

vortices. As already discussed previously, the width remains constant for any particular water depth even if the upstream flow velocity is varied.
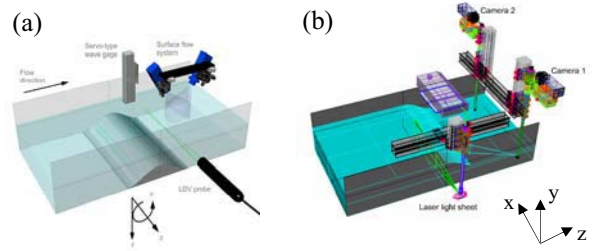
Figure 7. Experimental setup (a) Surface flow system, LDV and Wave gauge (b) 3D PIV system
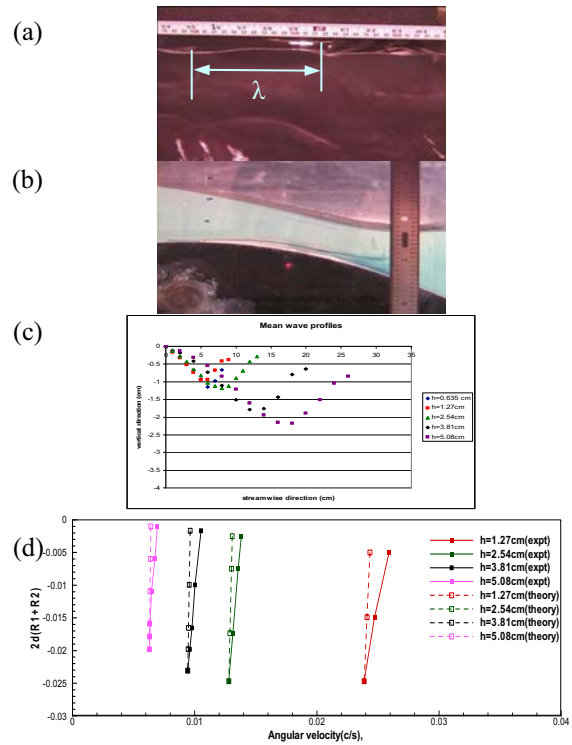
Figure 8. Experimental results (a) Wavelength of span-wise instability for h = 3.81 cm. (b) Gap width and separation line for h = 3.81 cm. (c) Free surface elevation profiles in the concave region. (d) Experimental and theoretical angular velocity profiles.

Values of gap width (d) are measured, by injecting dye into the flow (figure 8b) to observe the separation line along with a reference scale. The values of (d) measured this way are accurate enough for estimating values for a (a = $2\pi d/\lambda$). The free surface profiles in the concave region for different water depths measured with the wave gauge are shown in figure 8c. The radii of curvatures calculated from these profiles are quite repeatable and nearly exact. Laser Doppler

Velocimetry (LDV) is used to measure the velocity profiles within the gap between the free surface and the separation line. LDV velocity profiles are obtained in the vertical direction within the gap width.

At the separation line a sudden change in velocity is noticed which also helps to verify the values of gap widths that are estimated using video images. The mean flow theoretical velocity profile gives a lower velocity at the free surface than the separation line, but experiments show that the velocity is actually higher at the free surface. This results in the lower values of theoretical angular velocities as compared to experimental values at the free surface and can be seen in figure 8d. This is probably due to the assumption that u_θ is constant in θ direction, however, the experiments actually show variation of u_θ with θ which is caused by the acceleration of the flow over the bump. The velocity values at separation line for all water depths could have been estimated by using equation (15) and using the surface flow system only but it was decided to measure V_2 directly, where possible, to obtain more accurate measurements.

To further validate and quantify the vortex size and structures, digital particle image velocimetry (DPIV) measurements are obtained as shown in figure 7b. Two underwater cameras are used with a laser light sheet that is fired along the cross-plane to measure the instability vortices.
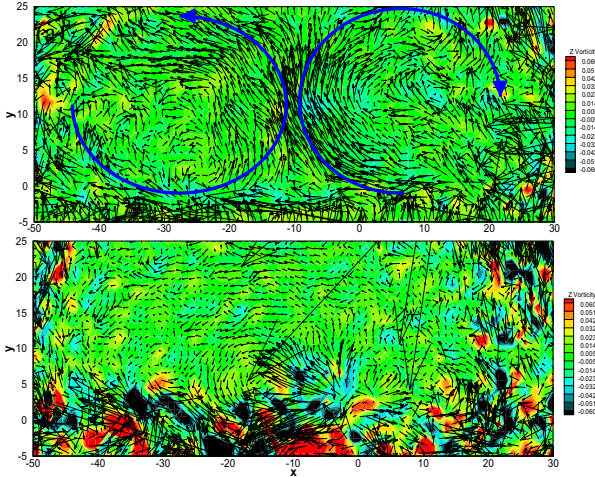
Figure 9. Cross-plane DPIV velocity vector plots for h = 3.81cm. First trough (z/H = 0.48) upstream of primary wave (top). 4 cm downstream (z/H = 0.83) of first trough (bottom).

The measurements are obtained at the trough of the primary wave and subsequently at more downstream locations. Figure 9 shows the velocity vectors that are calculated from cross correlation of DPIV images for h = 3.81cm. The presence of counter rotating stream-wise vortices in between free surface

and separation line caused by centrifugal instability is quite evident at the trough (figure 9a). The first trough is located upstream of the transition distance (table 3) for h = 3.81 cm and that is the reason why we do not see any shear layer vortices in figure 7a. As we move downstream of the transition distance (figure 9b) small scale incoherent stream-wise vortices can be observed near the separation line. The stream-wise vortices are formed due to the separated shear layer as discussed before (figure 4c). However, since these vortices are well below the free surface and much smaller in scale compared to the centrifugal stream-wise vortices, their effect on the free surface deformation is almost negligible. It is unclear as to why the centrifugal vortices are not distinctly seen in figure 9b. One of the possible reasons might be due to the low frame rate of the PIV cameras. The centrifugal vortices are spatially unsteady and move in the transverse direction with certain frequencies. Since the camera frame rate is very low (4.5 Hz) and the number of images obtained is 50, which is also insufficient, it is very likely that the PIV cameras missed the vortical structures in between the frames. For future experiments it is necessary to increase the camera frame rate and number of images to successfully measure the centrifugal vortices downstream of the trough. The centrifugal vortex sizes measured at the trough are consistent with the span-wise wavelength of instability measured from the scars at the free surface for all water depths, thus further confirming that the free surface instability is due to centrifugal force effect and not due to the shear layer instability.

The values of R_1, average centrifugal vortex width (w_T), gap width (d) and velocity at the separation line (V_2) have been used to calculate the experimental critical Taylor numbers for each water depth using equation (17). Table 4 summarizes the values for different experimental parameters and the calculated critical Taylor numbers.

Table 4. Critical Taylor numbers

Bump height = 11.43 cm					
h/H	0.056	0.111	0.222	0.333	0.444
w_T/W	0.006	0.011	0.035	0.060	0.120
$2d/(R_1+R_2)$	0.032	0.016	0.017	0.016	0.013
a	2.04	1.73	0.86	0.77	0.60
Re	814	1702	2861	5053	8171
Fr	0.529	0.512	0.586	0.646	0.782
We	159	1002	1693	5043	7079
η	0.968	0.984	0.983	0.988	0.987
Taylor(expt.)	2441	2955	9771	13754	44260
Taylor(theory)	2314	2685	7831	9583	14880

Note: Kinematic viscosity (v) = 1.5e-6 m^2/s. Experimental values of a, were calculated from vortex width (a = πd/w). $Re = V_2 d / v$, $Fr = \sqrt{gd}/V_1$, and $We = \rho V_1^2 R_1 / Y$, where. Y is the surface tension.

Uncertainties in experimentally determined critical Taylor numbers (table 5) are evaluated. The maximum percentage uncertainty is less than 5.54% and the experiments are quite repeatable starting from the initial conditions.

Table5. Bias limit, Precision limit and total Uncertainty for Taylor number evaluation.

		Bump size 11.43 cm		
h/D	Bias	Precision	Total uncertainty	% Uncertainty
0.111	82	48	94	3.19
0.222	245	90	261	2.67
0.333	309	70	317	2.31
0.444	2558	242	2570	5.54

Figure 10 shows the comparison of theoretical and experimental critical Taylor numbers for different water depths for both bumps. Theoretical Taylor curve is plotted with respect to (a) using equation (18). The flow is stable for all Taylor numbers below the theoretical solid curve for any value of (a) and the critical values which determine the onset of instability lie on the curve.
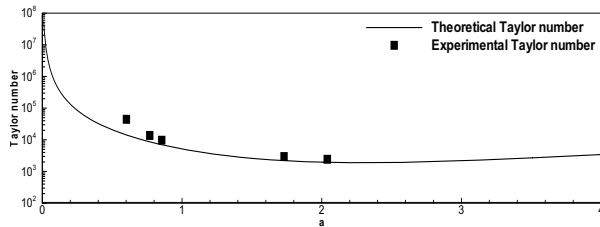
Figure 10. Critical Taylor number – comparison between experimental and theoretical values

The critical values from experiments are quite close to the predicted Taylor numbers. For water depths of 5 cm and higher, the instability span-wise wavelength increases significantly to almost 25% of the width of the flume and cannot be observed as distinctly as the lower depths. Hence the effect of the side walls cannot be ignored for such large span-wise vortices and current experimental results show deviation from predicted Taylor numbers.

Summary of instability analysis. Theoretical analysis followed by validation with experimental data for flow over the bottom bump, helped us achieve a solid physical understanding of otherwise a very complicated flow. Centrifugal instability analysis has been successfully used to predict critical Taylor number for free surface instability downstream of the bump. For water depths lower than 5.08 cm, the theory matches well with the experiments. For water depth 5.08 cm, the effect of the flume side walls might cause the deviation from expected results. For future it might

be interesting to conduct the same experiment in an open channel with larger aspect ratio and check if the side wall effects are eliminated. In addition to the centrifugal vortices, stream-wise vortices generated from the separating shear layer also exist downstream of the transition distance. However, since the sizes of the shear layer vortices are much smaller compared to the centrifugal vortices and the instability actually originates upstream of their transition distance, the shear layer vortices do not affect the free surface instability.

Even though good quality experimental data has been obtained for the estimates of vortex width from free surface photographs, gap widths and radius of curvatures of the free surface in the concave region, it will be worthwhile to obtain more extensive PIV measurements for all water depths in both cross-planes and planes parallel to the flow for different bump sizes. However, vector plots from PIV measurements at the trough have provided sufficient evidence of the existence of centrifugal vortices and their dominating effect in causing the free surface instability. PIV measurements further downstream were unable to properly capture the centrifugal vortices, which might be due to low camera frame rate and insufficient number of images. This will be improved in future experiments.

This present instability analysis might be extended to real life wave breaking on beaches, around ships and ocean structures. However, further studies are necessary to determine if these instabilities actually lead to deep or shallow water wave breaking and if so, then it can probably be used as an improved method for predicting the criteria for wave breaking. Rhee and Stern (2002) evaluated wave breaking criteria based on vertical pressure gradient, wave slope and wave steepness, but most of the current methods are largely empirical and it still remains an unresolved issue.

Periodic breaking
After evaluating the flow patterns with different bump sizes, it is found that increasing the bump size increases the wave height and so the largest bump size with optimum water depth (fourth order curvature bump of height 27.94cm and h = 3.81 cm) is chosen to generate the best plunging breaking wave. This also gives the desired wave height of 10 cm. As the speed is increased from the zero condition, at first a wave train is formed downstream of the bump with the primary wave being the largest. Free surface span-wise instabilities start appearing with slightly higher flow speed. As the speed is increased further these instabilities tend to merge together and form localized three dimensional plunging breakers. The breaking occurs at random span-wise locations and repeats itself after certain intervals. It is interesting to observe that

the span-wise location of this kind of periodic breaking can be controlled by introducing upstream disturbances close to the bump. The time interval between two successive breakers can also be controlled by controlling the timing of the upstream disturbance. At the instant of breaking the wave has a distinct triangular structure when viewed from the top. Figure 9 shows the top view of the wave as seen from the upstream direction.

Figure 11. Top-view of periodic wave breaking showing typical triangular structure.

Impulsive breaking

The flow conditions for impulsive breaking are very different from the periodic ones. Instead of maintaining a steady upstream flow speed, the flow is suddenly accelerated from zero to maximum value (0.7 m/s) over a period of few seconds. Only one single plunging breaker can be generated this way, after which the flow changes to a hydraulic jump and hence the term "impulsive". The breaking wave height, location and pattern is repeatable if the initial conditions are exactly the same. The bump height to water depth ratio is chosen according to Iafrati et. al 2001. The water height is varied with an attempt to obtain two dimensional plunging breaking that is repeatable, starting from the exact same initial conditions. The wave breaking phenomenon is found to be extremely sensitive to the initial conditions.
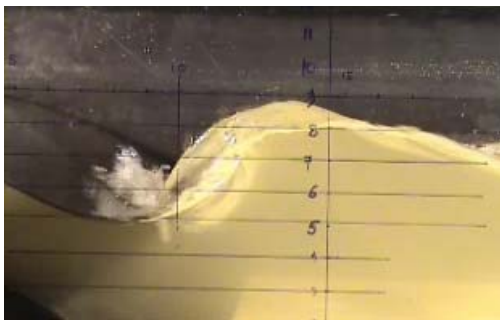
Figure 12. Side view of impulsive plunging breaker.

Sufficient time is given between two consecutive runs to ensure that the water in the flume is calm and free from any disturbance that can eventually

get magnified and affect the breaking. Three fourth-order curvature bumps of height 9cm, 11.4cm and 14cm are tested and finally the 11.43cm bump with h = 11.43cm gave the best results with wave height about 10 cm. Detailed times series video snapshots and their comparison with CFD simulations are presented in the later section. Figure 10 shows an instantaneous photograph of the side view of an impulsive breaker.

TWO PHASE LEVEL SET COMPUTATIONS & GHOST FLUID CFD

Background

As discussed in the general introduction, an important class of moving interface problems is encountered in the study of ship hydrodynamics, where free surface turbulent flow around submerged bodies (bumps, foils, submarines, etc.) or surface-piercing bodies (surface ships) constitute a challenge. Breaking waves, bubble entrainment, drop formation and air/wave interactions further complicate the problem. Basic research in this field concentrates on features such as air forces on the ship, air induced waves, vortex structures, and wakes both in water and air near the interface and the solid walls, etc. Some factors make computation of these problems especially difficult, in particular the singularity caused by large air/water density and viscosity ratios, very high Reynolds numbers with the resulting very thin boundary layer, complex geometries and free surface topologies.

Computations about the above problems have been done including single-phase or two-phase models and numerical methods. For example, Vogt and Larsson (1999), Iafrati et al. (2001), studied the free surface flow above submerged bump or foil. Hochbaum et al. (1999, 2000, 2002), Carrica and Wilson et al. (2004, 2006), Mascio et al. (2006) computed 3D turbulent flow around ship. Iafrati at al. (2001, 2005), Christensen et al., (2006) studied spilling or plunging wave breaking phenomena. Reddy et al. (2000) and Syms (2004) simulated air-wakes only in air region by assuming flat air/water interface as a computational boundary. However, further work is necessary to implement the detailed air/water flow, and improve the computation of air wakes by using completely coupled simulation both in air and water region while, considering ship deck and configuration and motion of real air/water free surface.

In this part of the paper we discuss two two-phase level set methods as applied to turbulent free surface flows: the classic Heaviside Function Method (HFM) and the Ghost Fluid Method (GFM) (Fedkiw et al., 1999,), (Kang et al., 2000), (Liu et al., 2000). On the HFM the fluid density and viscosity vary smoothly across the interface, while the GFM is characterized by a sharp interface. This last property makes GFM

specially suited for complex free surface 3D problems, in which relatively coarse grids need to be used. While HFM has been used for curvilinear coordinates (Hochbaum and Vogt 2002), the implementation of GFM for body-fitted structured grids is significantly more complex and is introduced in this paper. We present some 2D calculations with both the HFM and the GFM, and demonstrate the superiority of the second method. We then use the GFM to compute the air/water flow around a surface combatant. As opposed to previous computations of ship flows using two-phase level set, that were concerned only with the water flow, this example solves simultaneously the water flow around the hull and the air flow around an essentially flat deck. We also discuss the implementation of the Fast Marching Method with close point re-initialization algorithm in curvilinear grids.

Mathematical model

A single-fluid with variable properties is adopted to compute the immiscible and incompressible two-phase flow, therefore both phases (air and water) are advected with a common velocity. The mass and momentum conservation equations are as follows:

$$\nabla \cdot \mathbf{U} = 0 \tag{19}$$

$$\rho \frac{\partial \mathbf{U}}{\partial \tau} + \rho \nabla \cdot (\mathbf{U}\mathbf{U}) = -\nabla p +$$
$$\nabla \cdot \left[\frac{1}{Re_{eff}} \left((\nabla \mathbf{U}) + (\nabla \mathbf{U})^T \right) \right] + \mathbf{F} \tag{20}$$

The effective Reynolds number Re_{eff} is computed using a blended k - ω model (Menter 1994):

$$\rho \frac{\partial k}{\partial \tau} + \rho \nabla \cdot (\mathbf{U} k) = \nabla \cdot \left[\left(\frac{\mu}{Re} + \sigma_k \gamma_t \right) \nabla k \right] + S_k \tag{21}$$

$$\rho \frac{\partial \omega}{\partial \tau} + \rho \nabla \cdot (\mathbf{U} \omega) = \nabla \cdot \left[\left(\frac{\mu}{Re} + \sigma_k \gamma_t \right) \nabla \omega \right] + S_\omega \tag{22}$$

with $\mathbf{F} = \nabla \mathbf{z} (1 - \rho)/Fr^2$, $p = p* + z/Fr^2 + 2/3 \rho k$, $p*$ is the dimensionless absolute pressure, p the piezometric pressure (only in water), μ is the molecular viscosity, γ_t is the eddy viscosity, $Re = \rho_l U_0 L/\mu_l$, $Fr = U_0/\sqrt{gL}$, $\frac{1}{Re_{eff}} = \frac{\mu}{Re} + \gamma_t$, $\gamma_t = \rho \frac{k}{\omega}$, and S_k and S_ω are the sources of Eqs. (21) and (22). Surface tension is neglected for our large scale problems.

For the GFM method, the piezometric pressure is adopted for both fluids, and so some

modifications are necessary in equation (20), where piezometric pressure $p = p* + \rho z / Fr^2 + 2/3\rho k$, and F=0. We use level set function φ to capture the interface:

$$\frac{\partial \varphi}{\partial t} + \mathbf{U} \cdot \nabla \varphi = -\gamma \eta_w \tag{23}$$

Here, γ is an artificial wave damping function (Vogt and Larsson, 1999) and η_w is the wave elevation. On the HFM a Heaviside function is introduced

$$H(\varphi) = \begin{cases} 0 & if \ \varphi < -\varepsilon \\ (\varphi + \varepsilon)/2\varepsilon + \sin(\pi\varphi/\varepsilon)/2\pi & if \ |\varphi| \le \varepsilon \\ 1 & if \ \varphi > \varepsilon \end{cases} \tag{24}$$

where, ε is a prescribed "thickness" of the interface. The density and viscosity all over the domain are defined as follows,

$$\begin{cases} \rho(\mathbf{X}) = \rho_a + (\rho_l - \rho_a) H[\varphi(\mathbf{X})] \\ \mu(\mathbf{X}) = \mu_a + (\mu_l - \mu_a) H[\varphi(\mathbf{X})] \end{cases} \tag{25}$$

In addition, the modified δ function is written as:

$$\delta(\varphi) = \frac{dH}{d\varphi} = \begin{cases} [1 + \cos(\pi\varphi/\varepsilon)]/2\varepsilon & if \ |\varphi| < \varepsilon \\ 0 & if \ |\varphi| \ge \varepsilon \end{cases} \tag{26}$$

In contrast to the HFM, the GFM has a sharp free surface with zero transition thickness. The density and pressure satisfy the real jump conditions, the details are introduced in (Huang et al., 2006). The piezometric pressure jump conditions are:

$$[p] = [\rho] \frac{z_I}{Fr^2} \tag{27}$$

$$\left[\frac{\nabla p}{\rho} \right] = 0 \tag{28}$$

with z_I as the z value on the interface.

Numerical methods

The HFM and GFM algorithms were implemented in the code CFDShip-Iowa. The general algorithms used in CFDShip-Iowa are described in Carrica et al. (2006a and 2006b). For HFM algorithms, the fluid properties of the different fluids are included in the model. For GFM, we discuss how to enforce different fluids here.

We extend the GFM to curvilinear grids for free surface turbulent problems. First we transform

jump conditions of all variables into an arbitrary coordinate ξ. From Eq. (28), the jump condition of pressure in this direction can be written as

$$\left[\beta \frac{\partial p}{\partial \xi} \right] = 0 \qquad (29)$$

where $\beta = 1/\rho$. Secondly, we use appropriate numerical techniques to build the pressure matrix. Since, the pressure and pressure gradient are discontinuous across the interface for jump condition mentioned above, it causes an ill conditioned pressure matrix. Fedkiw et al. (1999) and Zhou et al. (2006) used fictitious points in the other fluid in a Cartesian grid to enforce the jump conditions. Following the ideas of Carrica et al. (2006a) for enforcing the interfacial pressure in a curvilinear grid with the single phase level-set method, we obtain a general expression for the ghost pressure on any neighboring point in a different fluid on curvilinear grids (figure 13). Combining Eqs. (27) and (29) for a point ijk and any neighbor in a different fluid mnk we obtain,

$$p_{mnk}^{G+} = \frac{\beta^-}{\bar{\beta}} p_{mnk} + \left(1 - \frac{\beta^-}{\bar{\beta}} \right) p_{ijk} - \frac{\beta^-}{\bar{\beta}} \frac{z_I}{Fr^2} [\rho] \qquad (30)$$

$$\bar{\beta} = (1 - \lambda) \beta^+ + \lambda \beta^- \qquad (31)$$

$$\lambda = \varphi_{ijk} / (\varphi_{ijk} - \varphi_{mnk}) \qquad (32)$$

This gives the ghost pressure in the neighboring point Q. By replacing Eq. (30) in the pressure matrix coefficient for the neighboring point we obtain new coefficients for the local and neighboring points, and an additional term for the RHS.
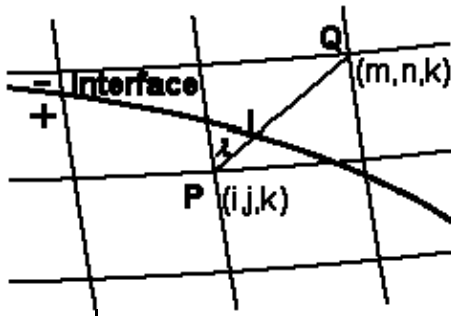

Figure 13. Jump conditions enforcement.

Furthermore, we implemented a projection method, and found that it was more consistent compared to PISO method to fit the pressure and its gradient jump condition. In addition, for simplicity, we assume that the viscosity and turbulent variables and their derivatives are continuous across the interface.

In order to keep the level set function a distance function at all times, we extend the re-initialization method of Adalsteinsson & Sethian (1999) to three dimensional curvilinear grids. The details are written in (Carrica et al., 2006a) and (Huang et al., 2006).

Computation examples

Plunging wave breaking above submerged bump. As a first test, we select an air/water impulsive plunging breaking wave with complex free surface topology. INSEAN's smooth bump (see Iafrati et al., 2001) is adopted. Only the HFM is used in this example. The topography of bump is given as follows,

$$z = -h + d(1 - 2\frac{x^2}{a^2} + \frac{x^4}{a^4}), \quad x \in (-a, a) \qquad (33)$$

where, h is the water depth, a is the bump half length and d is the bump height. The reference length is the bump's half length, and so $h = 0.844$, $a = 1$, $d = 0.4$. The 2D computational domain extends 28×2.844, with 461×191 grid points. Since CFDShip-Iowa is a 3D code, 5 grid points are used in the transverse direction. Initially the fluid is static, and the flow is suddenly accelerated from that state. Non-slip boundary conditions are used on the bump surface and bottom boundary, inlet, exit, and far field are set on other boundaries (Huang et al., 2006). Blended k-ε/k-ω and DES turbulence models (Xing et al., 2004) are used. A numerical beach is used in the upstream and downstream far regions to avoid wave reflections on the inlet and exit boundaries. The detailed evolution of the free surface computed by HFM and comparison with experimental results are presented in Figure 14.

The two phase results are able to capture the initial stages of plunging breaker, including the initial overturning of the wave, air entrapment, the first splash after the jet impact, the second splash when the remaining wave overturns, and matches well with experimental data. At the later stage the wave gets swept downstream and due to the presence of too many bubbles in the flow, it is difficult to visualize any distinct structures from EFD photographs and so comparison becomes more difficult.

Sub-critical flow over a bump. The sub-critical free surface flow over a bump is a typical problem to validate free surface methods. In this 2D problem the topography is (non- dimensionalized with bump length, Cahouet, 1984)

$$z = -h + \frac{27d}{4} x(x-1)^2 \qquad (34)$$

with h=0.5 the water depth, H=0.1 the bump height. The free surface is initially at z=0. The bump is placed at the bottom of a channel with still water, starts suddenly and evolves to a steady solution. The condition for Fr =0.304 and Re=3×10^5 was computed with single-phase level set, HFM and GFM with slip boundary condition, using inviscid or viscous model for the latter one. Computation domain is 17×2.1 with 245×111 grid points. The air/water density and viscosity ratios are 1.2×10^{-3} and 1.8×10^{-2}. Figure 15 shows a comparison of the free surface elevation between all methods and experiments. We can see that both the HFM and the GFM outperform the single-phase level set method for this test. However, for the velocity field, the HFM predicts the location of the vortices caused by the wave being too high, as shown in Figure 16. This is caused by the artificial thickness introduced in Eq. (24). This thickness cannot be set arbitrarily small but has to cover 5~10 grid points, thus resulting in a need for finer grids for the HFM compared to GFM.
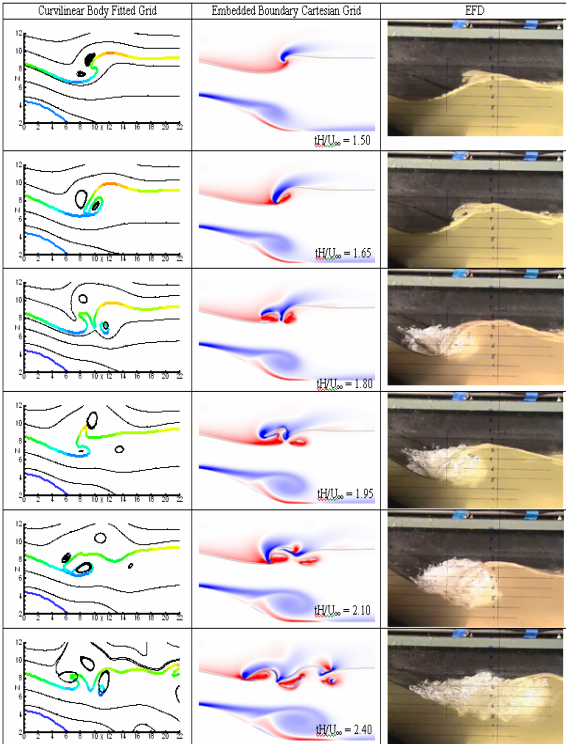

Figure 14. Comparison of CFD and EFD for impulsive plunging breaking wave profile with accelerated flow and smaller bump
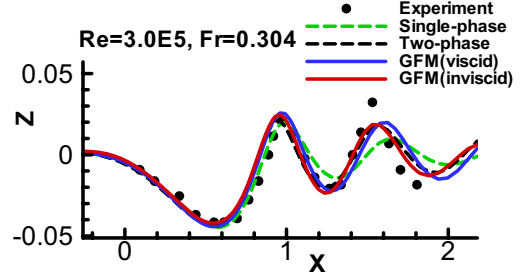
Figure 15. Wave elevation for a subcritical bump

Free surface turbulent flow around a ship model DTMB5512. Simulations were performed for a model surface combatant DTMB 5512 advancing in calm water at two Froude numbers, Fr=0.28 and Fr=0.41, corresponding to Reynolds numbers Re=4.85×10^6 and Re=710×10^6, respectively. The results for Fr=0.28 are compared with experiment data, and for Fr=0.41 the results are compared with single-phase computations in a fine grid. The air/water density and viscosity ratios are 1.2×10^{-3} and 1.8×10^{-2}. The GFM is used in this computation, enforcing jump conditions for the pressure and using smooth Heaviside functions for the momentum and turbulence equations. A relatively coarse double O grid is used from the hull surface to the far-filed boundary, with 615,000 grid points, distributed in 16 blocks. Inlet boundary conditions are used on the entire outer boundary, non-slip boundary condition is set on the ship hull, and symmetry condition is set on the y=0 plane. The computation starts impulsively from a static condition.
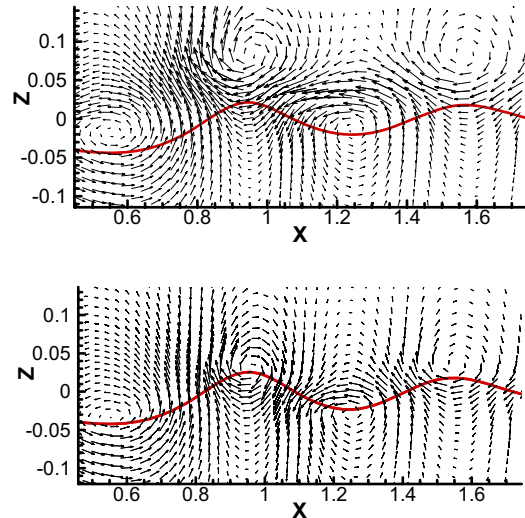
Figure 16. Velocity field for a subcritical bump. HFM (Top) GFM (Bottom)

From table 6, we can see the differences of resistances between experimental data and CFD.

Resistance values are small for both Fr numbers, wherein, the relative error is 4.77% and 5.65% for Fr=0.28 and Fr=0.41 respectively.

Table6. Resistance for DTMB 5512

	Experiment	CFD	Error (%)
Fr=0.28	0.00461	0.00483	4.77
Fr=0.41	0.00673	0.00711	5.65

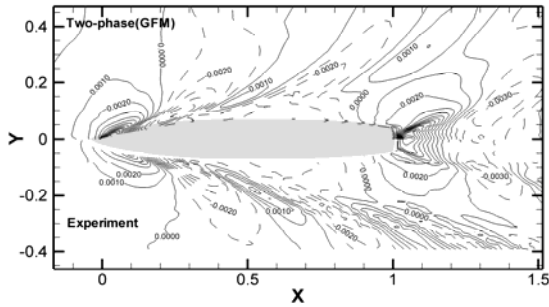The free surface elevation compared with experimental data for $Fr = 0.28$ is shown in Figure 17.

Figure 17. Wave elevation (Fr=0.28)

In Figure 18, we compare the two-phase computation for the case with $Fr = 0.41$ against single-phase results in a much finer grid (3.84 million points) with overset grids which is validated for some typical ship cases (there is no experimental data in the whole field for this case). The general results are good, though wave dissipation is observed in the far field, mainly for the Fr=0.28 case. This is to be expected for this level of refinement in a double-O grid. The Fr=0.41 case cannot capture the bow breaking wave, again as expected for this level of resolution, and thus differences are observed everywhere downstream.
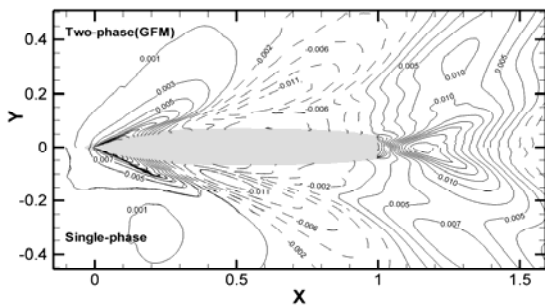

Figure 18. Wave elevation (Fr=0.41)

Figure 19 shows computational results and experimental data (Longo and Stern, 2005) for u velocity distribution in the nominal wake plane, with excellent agreement.
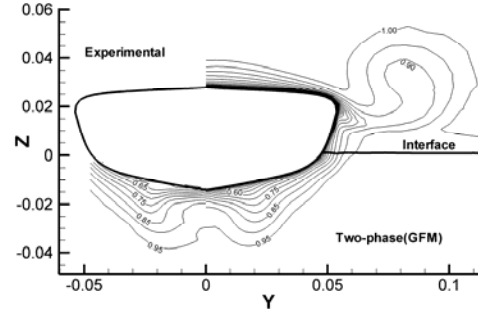

Figure 19. Axial velocity at nominal wake plane

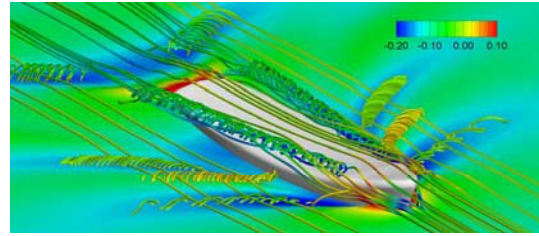**Figure 20.** Streamlines in the air region (Fr=0.28, front view). The streamlines are colored by axial velocity on the earth system, 13 levels: -0.20~0.10, free surface is colored by z value, 21 levels: -0.005-0.01, the local vortex is on the $Q = 10$ iso-surface.

Notice that the GFM computation predicts the flow field in the air region and near the interface. Figure 20 and 21 show the free surface and the streamlines in the air region for the cases with Fr=0.28 and Fr=0.41, respectively. Two types of streamlines are shown: both are colored by axial velocity in an earth fixed coordinate system. Notice the ability of the GFM to capture the orbital velocity caused by the waves, and vortices detaching from the bow region. These vortices cause a wake shown clearly in Figure 19.
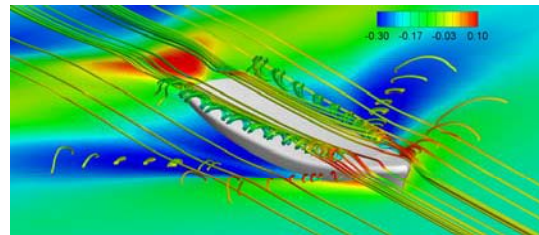

Figure 21. Streamlines in the air region (Fr=0.41, front view). The streamlines are colored by axial velocity on the earth system, 13 levels: -0.30~0.10, free surface is colored by z value, 21 levels: -0.01-0.02, the local vortex is on the $Q = 10$ isosurface.

Summary of two-phase level set computations. Two two-phase level set methods, HFM and GFM are extended to curvilinear body-fitted grid to simulate air/water free surface turbulent flows. The

methods are validated with three cases: plunging wave breaking, sub-critical free surface flows caused by a submerged bump, and free surface turbulent flow both in air and water region around a ship model DTMB 5512. The results for the sub-critical flow over the bump show that the GFM has superior performance for the grid spacing that is to be expected in ship computations, due to the explicit enforcement of the jump conditions. The HFM is limited by requirements of very fine discretization near the free surface. For all cases, the results are in good agreement with experimental data and corresponding single-phase level set computations. Although the two-phase method faces some difficulties caused by large density ratios, it can resolve the flow field in the air region.

TWO PHASE LEVEL SET EMBEDDED BOUNDARY CARTESIAN GRID APPROACH

Background
Wave breaking is an important subject in geophysics, coastal and marine engineering. Although significant progress in theoretical, experimental, and numerical aspects has been made during the past decade, several substantial characteristics of breakers in nature have not been investigated in detail. Among them are three dimensional effects, which present greater challenge to further studies, especially numerical ones, due to the exceptional demand for numerical methods and extensive computer power requirement.

Currently, we are developing a high-fidelity and cost-effective computational tool for the simulations of three-dimensional two-phase (air /water) turbulent flows involving complex stationary /moving solid boundaries and strong air/water interactions, i.e., breaking waves. The basic idea is to use a highly efficient Cartesian solver for the background flow field, while a curvilinear solver is used for the very thin boundary layer attaching the ship hull. The communication between these two solvers is done via the sophisticated overset grid tool SUGGAR. As a first step, we shall demonstrate the development of our Cartesian solver for complicated two-phase flows in this paper. And instead of the curvilinear solver linked by SUGGAR, an embedded boundary method is adopted for the immersed bodies. This method was originated by Peskin (1972), in which the effects of solid/elastic boundaries on the fluid are modeled by a set of body forces distributed over the nearby flow field of the immersed boundaries. In Fadlun et al. (2000) the concept of body forcing was also adopted, however, in a discrete manner and a sharp interface was obtained. The latter, i.e., the so-called direct forcing approach, has gained increased popularity in recent years (see Mittal and Iaccarino 2005 for a review). In these methods, usually a linear/quadratic distribution of the

velocity near the wall is assumed and the first grid point away from the wall needs to be in the viscous sublayer for turbulence flow calculations. Therefore, high Reynolds number flow simulations using embedded boundary methods require enormous grid points near the wall. As a result of this limitation, here we only show two cases at low and moderate Reynolds numbers, although high Reynolds number flows can be easily calculated by adding turbulence models and wall models into the current embedded boundary Cartesian grid approach: the two-dimensional plunging breaking waves by a surface-mounted bump discussed in the previous sections (also in Iafrati et al. 2001) and the non-breaking waves generated by a fully submerged NACA 0012 hydrofoil (Duncan 1983).

Computational method
The level set formulation for the incompressible flows of two immiscible fluids separated by an interface given by Chang et al (1996) is used here. In this approach, one set of equations for both fluids are solved with the density and viscosity jumps across the interface smoothed by a Heaviside function. The surface tension is modeled as a distributed singular force around the interface. The smooth Heaviside function and Dirac delta function are based on the level set function. The equations used in this part are given in previous CFD section with no contribution to Re_{eff} from turbulence models, i.e., $\gamma_t = 0$. The level set function is evolved using an Eulerian convection equation and reinitialized using a similar equation given by Sussman et al (1994) to keep the level set as a distance function. Here we adopt the local (narrow band) level set method by Peng et al (1999) for the level set and the re-initialization equations.

The embedded boundary formulation by Yang and Balaras (2006) is adopted here to treat the immersed boundaries/bodies in a non-uniform Cartesian grid. In this approach, the grid generation for complex geometries is trivial as the requirement that the grid points coincide with the boundary, which is imperative for body-fitted methods, is relaxed; while the solution near the immersed boundary is reconstructed using momentum forcing in a sharp-interface manner. Due to the fact that the grid lines do not align with the immersed boundaries, in order to capture the thinner boundary layer for higher Reynolds number, the Cartesian grid has to be refined in more than one direction and usually more grid points are required comparing with body fitted grids. Both local grid refinement and wall layer modeling techniques are necessary for embedded boundary approach to be applied in the computations of high Reynolds number flows in naval hydrodynamics.

A fractional step method is used to solve the Navier-Stokes equations. The spatial discretization

methods use are the standard second-order central difference schemes for the Navier-Stokes equations on a staggered grid and fifth order WENO scheme for the convective terms. The time advancement scheme is a semi-implicit second-order Crank-Nicolson scheme for the diagonal viscous terms and second-order Adams-Bashforth scheme for the convective and other terms. The parallelization is done via a domain decomposition technique (slab decomposition in streamwise direction) using the MPI library. We use the parallel tridiagonal system solver given by Mattor et al (1995) for tridiagonal linear equations rising from the momentum equations and the multigrid solver from PETSc library (Balay et al., 1997) for pressure Poisson equation.

The level set and the reinitialization equations are solved using third order TVD Runge-Kutta scheme (Shu and Osher 1988) for time advancement and fifth-order HJ WENO scheme (Jiang and Peng, 2000) for spatial discretization. The additional solutions of these equations do not pose a significant overhead as they are solved in a narrow band about several grid-cell wide.

At each time step, the level set equation is first solved to advance the interface position, then the reinitialization equation is iterated (usually, 2 iterations) to keep the level set function as a good approximate of the signed distance function. With this new interface position (zero level set), the density and viscosity of two different phases are smoothed across the interface. Then the immersed boundaries are defined and embedded boundary information is set up (note this step is done only once for stationary body problem). With the above information, the momentum equations are solved with a pressure field from the previous time step to give a predicted velocity field, which is not divergence free. Thus, a Poisson equation for the pressure correction is formed and solved using a multigrid method via PETSc. With the pressure correction the velocity and pressure fields are updated to the current time step.

The solution of Poisson equation is the most expensive part and takes more than 90 per cent of the CPU time. Here a tight convergence criterion for the Poisson equation, the relative residual norm $|\varepsilon|_2 \leq 10^{-12}$, is used. With three grid levels and GMRES as the smoother one, the PETSc multigrid solver can converge in around 15 iterations for the two-dimensional cases presented here. The average CPU cost is about 1.5×10^{-4} second per (grid-point time-step) on the NAVO MSRC IBM Cluster 1600 equipped with 1.7GHz Power4+ processors.

Breaking wave simulation. In this part we demonstrate the application of our level set/embedded boundary Cartesian grid approach in the breaking wave simulations.
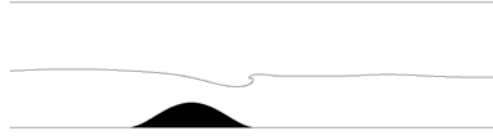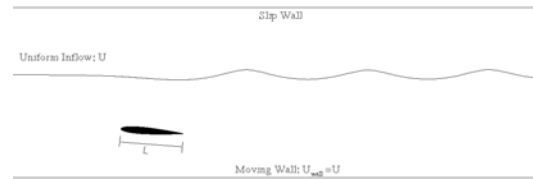

Figure 22. Computational domain for breaking waves over a surface-mounted bump.

Figure 22 gives the schematic of the computational setup for the impulsive plunging breaking waves behind a surface mounted bump, which have been studied both experimentally and calculated using body-fitted grid in previous parts.

The computational domain is $24L \times 2L$ and the number of grid points is 1024×512 in the streamwise and cross-stream directions, respectively. A simulation has been performed at Re = 1, 000 and Fr = 0.317 based on the bulk inflow velocity and half bump length. Figure 14 (shown previously) gives the instantaneous breaking wave profiles and vorticity contours at several instances.

Submerged hydrofoil simulation. Here we only show a preliminary two dimensional simulation of the non-breaking wave by a submerged hydrofoil. The computational domain, $19L \times 3L$ in the streamwise and cross-stream directions, respectively, with L the hydrofoil chord length, is shown in Figure 23 and the corresponding grid points used are 1024×448.


Figure 23. Computational domain for a submerged hydrofoil in a uniform flow.

The Reynolds number based on the uniform inflow velocity U and the hydrofoil chord length L is $\mathrm{Re} = UL/\nu = 5 \times 10^4$ with ν the kinematic viscosity of the liquid phase, which is lower than that in the experiment 1.624×10^5 (Duncan 1983). The Froude number $\mathrm{Fr} = U/\sqrt{gL} = 0.5672$. The hydrofoil has a constant positive attack angle $\alpha = 5°$ and a constant depth of submergence at the mid-chord position, $d_s = 0.951$. The boundary conditions shown in Figure 23 are used. The comparison of wave profiles from the experiment and the present simulation are quite good as given in Figure 24, except for the fact that the simulation under predicted the first wave.
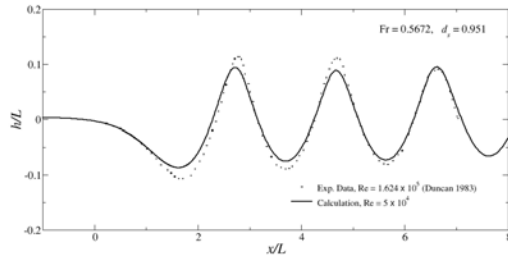
**Figure 24.** Wave profile generated by a submerged hydrofoil.
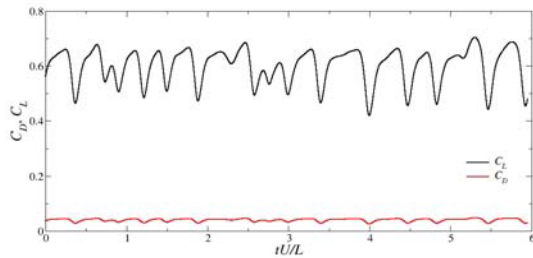
Figure 25. Time series of drag and lift coefficients for a submerged hydrofoil.

Figure 25 shows the time history of the drag and lift coefficients. An instantaneous snapshot of the vortices shed from the hydrofoil is presented in Figure 26 and the corresponding close-up around the hydrofoil is given in Figure 27. The vortex shedding pattern is very similar to the $Re = 3 \times 10^4$ case by Chen and Chwang (2002). However, a feature missed in their results is the surface vorticity distribution as they solved only for the liquid phase.
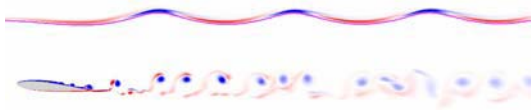
Figure 26. Instantaneous vorticity contours. Purple line identifies the free surface.
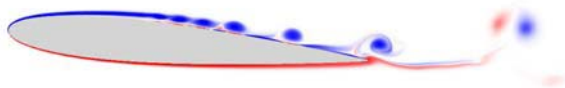
Figure 27. A close-up view of the vorticity distribution near the hydrofoil

CONLCUDING REMARKS

The optimum flow parameters and conditions for generating both periodic and impulsive plunging wave breaking were achieved after detailed experimental studies with different bump sizes and water depths in the open channel flume. While impulsive breaking is mostly two dimensional, periodic breaking is characterized by span-wise free surface instability at low upstream flow velocities prior to the breaking process. A critical non-dimensional Taylor number that determines the onset of this instability is derived from theoretical analysis and the theoretical predictions matched well with the experimental values. Future work will mainly focus on actual wave breaking measurements including turbulence velocity and vorticity fields for both 2D and stereo PIV measurements to properly characterize the entire 3D flow field around a plunging breaker for both periodic and impulsive breaking and the experimental data will be compared with CFD results.

The HFM has been implemented into a modified version of the curvilinear grids solver CFDShip-Iowa. An unsteady plunging breaking wave and a subcritical bump were computed with this method, showing good agreement with experimental data. A novel implementation of the GFM to curvilinear grids was presented, where the jump conditions are enforced explicitly whenever any of the neighbors in a 19 point stencil is in a different fluid. This method was used first to compute the subcritical free surface flow over a bump.

The comparison of results between HFM and GFM for the flow over a bump clearly shows that the transition region seriously limits the accuracy of the HFM method if the grids are not very fine. The ability of the GFM to maintain a sharp interface greatly benefits computations where the grids are not extremely fine. On the other hand, HFM is easier to implement and its robustness can be increased by enlarging the transition region (at the cost of accuracy). This motivated our selection of GFM as the method to implement into CFDShip-Iowa version 5, a curvilinear two-phase solver.

The GFM was used to solve the air/water flow around a DTMB 5512 model with an essentially horizontal deck. The CFD results are promising and compare well with the experimental data. One of the drawbacks of the GFM is the complexity involved in adding overset capability. This task is currently under way. Other areas of current and future work include implementation of a second-order interpolation to enforce the pressure jump conditions, implementation of the jump conditions will be implemented for viscosity, velocity gradients and turbulent quantities, and link to the full capabilities of CFDShip-Iowa version 4.

The two-phase level set embedded boundary Cartesian grid method was presented. The method has proven to be very efficient and accurate as higher-order schemes and scalable multigrid Poisson solvers have

been easily implemented. Computational results obtained for a submerged hydrofoil and an unsteady bump flow show the potential of the method. In three dimensional simulations, a wall modeling technique similar to that by Tessicini et al. (2002) for embedded boundary methods will be implemented and validated to capture the effects of thin boundary layers at high Reynolds numbers. For very high Reynolds numbers body fitted grids will be necessary, and thus an overset or hybrid grid approach, which combines the advantages of Cartesian and curvilinear solvers, is imperative in the near future. This approach has enormous potential and is being explored, both for single-phase and two-phase level set codes. The expected improvement with respect to computational cost can be one order of magnitude.

ACKNOWLEDGEMENTS

REFERENCES

Adalsteinsson, D., and Sethian, J.A., "The Fast Construction of Extension Velocities in Level Set Method," J. Comput. Phys., Vol. 148, 1999, pp. 2-22.

Balay, S., Gropp, W.D., McInnes, L.C., Smith, B.F., "Efficient Management of Parallelism in Object Oriented Numerical Software Libraries," in Modern Software Tools in Scientific Computing, Edited by E. Arge, A.M. Bruaset, H.P. Langtangen, Birkḧauser Press, 1997, pp. 163–202.

Cahouet. J., "Etude Numerique er Experimentale du Probleme Bbidimensionnel de la Resistance de Vaques Non-Lineaire," Ph.D. Thesis, ENSTA, Paris, 1984 (in French)

Carrica, P.M., Wilson, R.V., Stern, F., "An Unsteady Single-Phase Level Set Method for Viscous Free Surface Flows," Int. J. Num. Methods Fluids, 2006 (in press)

Carrica, P.M., Wilson, R.V., Stern, F., "Unsteady RANS Simulation of the Ship Forward Speed Diffraction Problem," Computers & Fluids, Vol. 35, 2006, pp. 545-570.

Chandrasekhar, S. Hydrodynamic and Hydromagnetic Stability. Dover publications, New York, 1961.

Chang, Y.C., Hou, T.Y., Merriman, B., et al., "A Level Set Formulation of Eulerian Interface Capturing Methods for Incompressible Fluid Flows," J. Comp. Phys. Vol. 124, 1996, pp. 449–464.

Chen, T., and Chwang, A.T., "Trailing Vortices in a Free-surface Flow," Phys. Fluids, Vol. 14, 2002, pp. 827–838.

Christensen, E.D., "Large Eddy Simulation of Spilling and Plunging Breakers," Coastal Engineering, Vol. 53, 2006, pp. 463-485.

Dong, R. R., Chu, S., and Katz, J., "Quantitative Visualization of the Flow Structure Within the Volute of a Centrifugal Pump, Part A: Technique," Trans. ASME: J. Fluids Eng. Vol. 114, 1992, pp. 390.

Duncan, J.H., "The Breaking and Non-breaking Wave Resistance of a Twodimensional Hydrofoil," J. Fluid Mech., Vol. 126, 1983, pp. 507–520.

Fadlun, E.A., Verzicco, R., Orlandi, P., Mohd-Yusof, J., "Combined immersed-boundary finite-difference methods for three-dimensional complex flow simulations," J. Comput. Phys., Vol. 161, 2000, pp. 35-60.

Fedkiw, R., Aslam, T. and Xu, S., "The Ghost Fluid Method for Deflagration and Detonation Discontinuities," J. Comp. Phys., Vol. 154, 1999, pp. 393-427.

Hochbaum, A. C., Shumann, C., "Free Surface Viscous Flow around Ship Models," 7th Int. Conf. Numerical ship Hydrodynamics, Nantes, France 1999.

Hochbaum, A. C., Vogt, M., "Flow and Resistance Prediction for a Container Ship," Pro. Gothenburg 2000, A Workshop on CFD in ship Hydrodynamics, Gothenburg, Swenden, 2000.

Hochbaum, A. C., Vogt, M., "Towards the Simulation of Seakeeping and Maneuvering Based on the Computation of the Free Surface Viscous Ship Flow," 24th ONR Symp. On Naval Hydrodynamics, Fukoka, Japan 2002.

Huang, J., Carrica, P.M., Stern, F., "Coupled Ghost Fluid Method and Two-Phase Level Set Method in the Curvilinear Body Fitted Grid," 2006. Manuscript in preparation.

Iafrati, A., Di Mascio A., and Campana, E.F., "A Level Set Technique Applied to Unsteady Free Surface Flows," Int. J. Num. Meth. Fluids, Vol. 35, 2001, pp. 281-297.

Iafrati, A., Campana, E.F., "Free-Surface Fluctuations and Behind Microbreakers: Space-Time Behaviour and Subsurface Flow Field," J. Fluid Mech., Vol.000, 2005, pp. 1-37.

Jiang, G.-S., Peng, D., "Weighted ENO Schemes for HamiltonJacobi Equations," SIAM J. Sci. Comp., Vol. 21, 2000, pp. 2126-2143.

Kang, M., Fedkiw, R. and Liu, X. D., "A Boundary Condition Capturing Method for Multiphase Incompressible Flow," J. Sci. Comp., Vol. 15, 2000, pp. 323-360.

Kirkil, G. & Constantinescu, G., "Investigation of Turbulent Flow Field around a Circular Cylinder on Flat Bed using Large Eddy Simulation," 2006, Manuscript in preparation.

Lin, J. C. and Rockwell, D., "Evolution of a Quasi-Steady Breaking Wave," J. Fluid Mech., Vol. 302, pp. 29.

Liu, X. D., Fedkiw, R. and Kang, M., "A Boundary Condition Capturing Method for Poisson's Equation on Irregular Domains," J. Comp. Phys., Vol. 160, 2000, pp. 151-178.

Longo, J., and Stern, F., "Uncertainty Assessment for Towing Tank Tests With Example for Surface Combatant DTMB Model 5512," J. Ship Research, Vol. 49, No. 1, 2005, pp. 55-68.

Mansy, H., Yank, P. and Williams, D. R., "Quantitative Measurements of Spanwise-periodic Three-dimensional Structures in the Wake of a Circular Cylinder," J. Fluid Mech., Vol. 270, 1994, pp. 277.

Mascio, A. D., Broglia, R., Muscari, R., "A Single-Phase Level Set Method for Solving Viscous Free Surface Flows," Int. J. Num. Meth. Fluids, 2006 (in press).

Mattor, N., Williams, T.J., Hewett, D.W., "Algorithm for Solving Tridiagonal Matrix Problems in Parallel," Parallel Computing, Vol. 21, 1995, pp. 1769–1782.

Menter, F. R., "Two-Equation Eddy Viscosity Turbulence Models for Engineering Applications," AIAA Journal, Vol.32, 1994, pp.1598-1605.

Mittal, R., Iaccarino, J., "Immersed Boundary methods," Annu. Rev. Fluid Mech., Vol. 37, 2005, pp. 239-26.

Miyata, H., and Inui, T., "Nonlinear Ship Waves," Adv. Appl. Mech., Vol. 24, 1984, pp. 215.

Peng, D., Merriman, B., Osher, S., Zhao, H., and Kang, M., "A PDE-Based Fast Local Level Set Method," J. Comp. Phys., Vol. 155, 1999, pp. 410–438.

Peregrine, D. H. "Breaking Waves on Beaches," Ann. Rev. Fluid Mech. Vol. 15, 1983, pp. 149-178.

Perlin, M., He, J., and Bernal, L. P., "An Experimental Study of Deep Water Plunging Breakers," Phys. Fluids, Vol. 8 (9), 1996, pp. 2365-2374.

Peskin, C. S., "Flow patterns around heart valves: a numerical method," J. Comp. Phys., Vol. 10, 1972, pp. 252-271.

Pogozelski, E. M., Katz, J. and Huang, T. T., "The Flow Structure around a Surface Piercing Strut," Phys. Fluids, Vol. 9, 1997, pp. 1387.

Reddy, K.R., Toffoletto, R., Jones, K.R.W., "Numerical Simulation of Ship Airwake," Computers & Fluids, Vol. 29, 2000, pp. 451-465.

Reid, W. H., "Inviscid Modes of Instability in Couette Flow," J. Math. Anal. and Appl. Vol. 1, 1960, pp. 411-422.

Rhee, S. H. and Stern, F., "RANS Modeling for Spilling Breaking Waves," J. Fluids Engineering, Vol. 124, 2002, pp. 424-432.

Sato, H., "Experimental Investigation on the Transition of Laminar Separated Layer," J. Phys. Soc. Jpn. Vol. 11, 1956, pp. 702.

Shu, C. W. and Osher, S., "Efficient Implementation of Essentially Non-oscillatory Shock-capturing Schemes," J. Comp. Phys. Vol. 77, 1988, pp. 439–471.

Steinbach, T., Liu, X., and Duncan, J. H. "Cross-stream Crest Profiles of Gentle Spilling Breakers," Advances in Coastal and Ocean engineering: Interaction of strong turbulence and with free surfaces, Vol. 8, 2002, pp. 43-63.

Sussman, M., Smereka, P., and Osher, S., "A Level Set Approach for Computing Solutions to Incompressible Two-Phase Flow," J. Comp. Phys., Vol. 114, 1994, pp. 146–159.

Syms, GF., "Numerical Simulation of Frigate Airwakes," Int. J Comp. Fluid Dynamics, Vol. 18, 2004, pp. 199-207.

Tessicini, F., Iaccarino, G., Fatica, M., Wang, M., and Verzicco, R., "Wall Modeling for Large-eddy Simulation Using an Immersed Boundary Method," Annual Research Briefs , 2002, Center for Turbulent Research.

Vogt, M., and Larsson, L., "Level Set Method for Predicting Viscous Free Surface Flows," 7th Int. Conf. Numerical ship Hydrodynamics, Nantes, France 1999.

Williamson, C. H. K. "Vortex Dynamics in the Cylinder Wake," Ann. Rev. Fluid Mech. Vol. 28, 1996, pp. 477-539.

Wilson, R.V., Carrica, P.M., Hyman, M., and Stern, F., "A Single-Phase Level Set Method with Application to Breaking Waves and Forward Speed Diffraction Problem," 25th Symposium on Naval Hydrodynamics. St. John's, Newfoundland and Labrador, Canada, 2004. pp. 8-13.

Xing, T., Kandasamy M., Wilson R., and Stern F., "DES and RANS of Unsteady Free-Surface flows," In proceedings of the 42nd AIAA aerospace sciences meeting, Reno, Nevada, Division for Fluid Dynamics. 2004.

Yang, J., and Balaras, E., "An Embedded-boundary Formulation for Large-eddy Simulation of Turbulent Flows Interacting with Moving Boundaries," J. Comp. Phys., Vol. 215, 2006, pp. 12–40.

Zhou, Y.C., Zhao, S., Feig, M., and Wei, G.W., "High Order Matched Interface and Boundary Method for Elliptic Equations with Discontinuous Coefficients and Singular Sources," J. Comp. Phys., Vol. 213, 2006, pp. 1-30.